NANO LETTERS

Letter

pubs.acs.org/NanoLett

Domain Wall Geometry Controls Conduction in Ferroelectrics

R. K. Vasudevan,[†] A. N. Morozovska,[‡] E. A. Eliseev,[§] J. Britson,[∥] J.-C. Yang,[⊥] Y.-H. Chu,[⊥] P. Maksymovych,[#] L. Q. Chen,[∥] V. Nagarajan,*[,†] and S. V. Kalinin*[,#]

[†]School of Materials Science and Engineering, University of New South Wales, Kensington 2052, Australia

[‡]Institute of Physics of National Academy of Sciences of Ukraine and [§]Institute of Problems of Material Science of National Academy of Sciences of Ukraine, 03028, Kiev, Ukraine

[∥]Department of Materials Science and Engineering, The Pennsylvania State University, University Park, Pennsylvania 16802, United States

[⊥]Department of Materials Science and Engineering, National Chiao Tung University, Hsinchu, Taiwan 30010

[#]The Center for Nanophase Materials Sciences, Oak Ridge National Laboratory, Oak Ridge, Tennessee 37831, United States

Supporting Information

ABSTRACT: A new paradigm of domain wall nanoelectronics has emerged recently, in which the domain wall in a ferroic is itself an active device element. The ability to spatially modulate the ferroic order parameter within a single domain wall allows the physical properties to be tailored at will and hence opens vastly unexplored device possibilities. Here, we demonstrate via ambient and ultrahigh-vacuum (UHV) scanning probe microscopy (SPM) measurements in bismuth ferrite that the conductivity of the domain walls can be modulated by up to 500% in the spatial dimension as a function of domain wall curvature. Landau−Ginzburg−Devonshire calculations reveal the conduction is a result of carriers or vacancies migrating to neutralize the charge at the formed interface. Phase-field modeling indicates that anisotropic potential distributions can occur even for initially uncharged walls, from polarization dynamics mediated by elastic effects. These results are the first proof of concept for modulation of charge as a function of domain wall geometry by a proximal probe, thereby expanding potential applications for oxide ferroics in future nanoscale electronics.

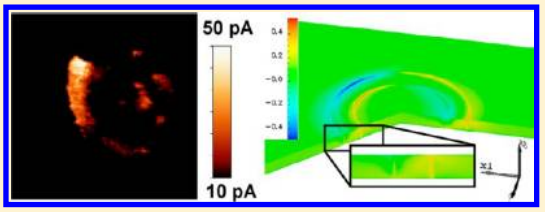

KEYWORDS: *Domain wall conduction, PFM, phase-field modeling, c-AFM, ferroelectrics*

The discovery of novel electronic, magnetic, and superconductive functionalities at domain walls,[1−4] where the walls have physical properties distinct from the domains has led to a radically new notion: that the device may be governed not so much by the properties of the domains, but those of the domain walls.[5] Domain wall engineering opens pathways to control a vast array of interfacial physical phenomena such as band structure manipulation,[6] ferroelastic transitions,[7] band gap narrowing due to intrinsic symmetry changes,[8] point-defect migration,[9,10] and order parameter couplings[11−14] that are not exhibited by the parent bulk phase. While it has been known theoretically that properties of domain walls can differ drastically from the bulk phase, it is only recently that experimental techniques to probe the properties at the individual domain wall level have been realized.[2,7,15−19] Yet, exploitation of the unique functional properties of domain walls to open new device frontiers hinges on the ability to tailor the properties at the individual wall level.

For ferroelectrics, Guro et al.[20] predicted that charged domains walls in large band gap semiconductors will possess significant charge and induce accumulation or inversion in adjacent regions of the material. This work has recently been extended by several groups to provide a comprehensive theoretical description[21] in both uniaxial[22] and multiaxial[23] ferroelectrics. The total amount of charge can be sufficient to induce onset of local conductivity in different nonconductive materials, as directly visualized for conductive channels at 109° and 180° ferroelastic domain walls in $BiFeO_3$.[2] Following this report, conductivity was demonstrated for other types of domain walls in $BiFeO_3$,[15] and domain walls in $Pb(Zr,Ti)O_3$,[19] suggesting that this behavior is universal for ferroelectrics. Furthermore, detailed studies of conductivity at the walls have demonstrated an intriguing set of hysteretic[16] and memory effects and time dynamics.[22] These observations suggest that domain wall conductance is a dynamic process that is intrinsically linked to slow polarization dynamics (i.e., evolution of wall shape[24,25]) or slow ionic processes such as carrier/vacancy segregation processes (e.g., compare to recent studies at metal-ferroelectric junctions[6,26]). Realistically, both mechanisms can be active and strongly coupled. As such, the geometry of the domain wall, specifically the presence of polarization discontinuities, is therefore an important physical parameter that is not yet well understood experimentally. Additionally, the tantalizing possibility of tailoring the properties of the individual domain wall in a standard ferroelectric,

Received: June 26, 2012
Revised: September 18, 2012
Published: September 20, 2012

   dx.doi.org/10.1021/nl302382k | *Nano Lett.* 2012, 12, 5524−5531

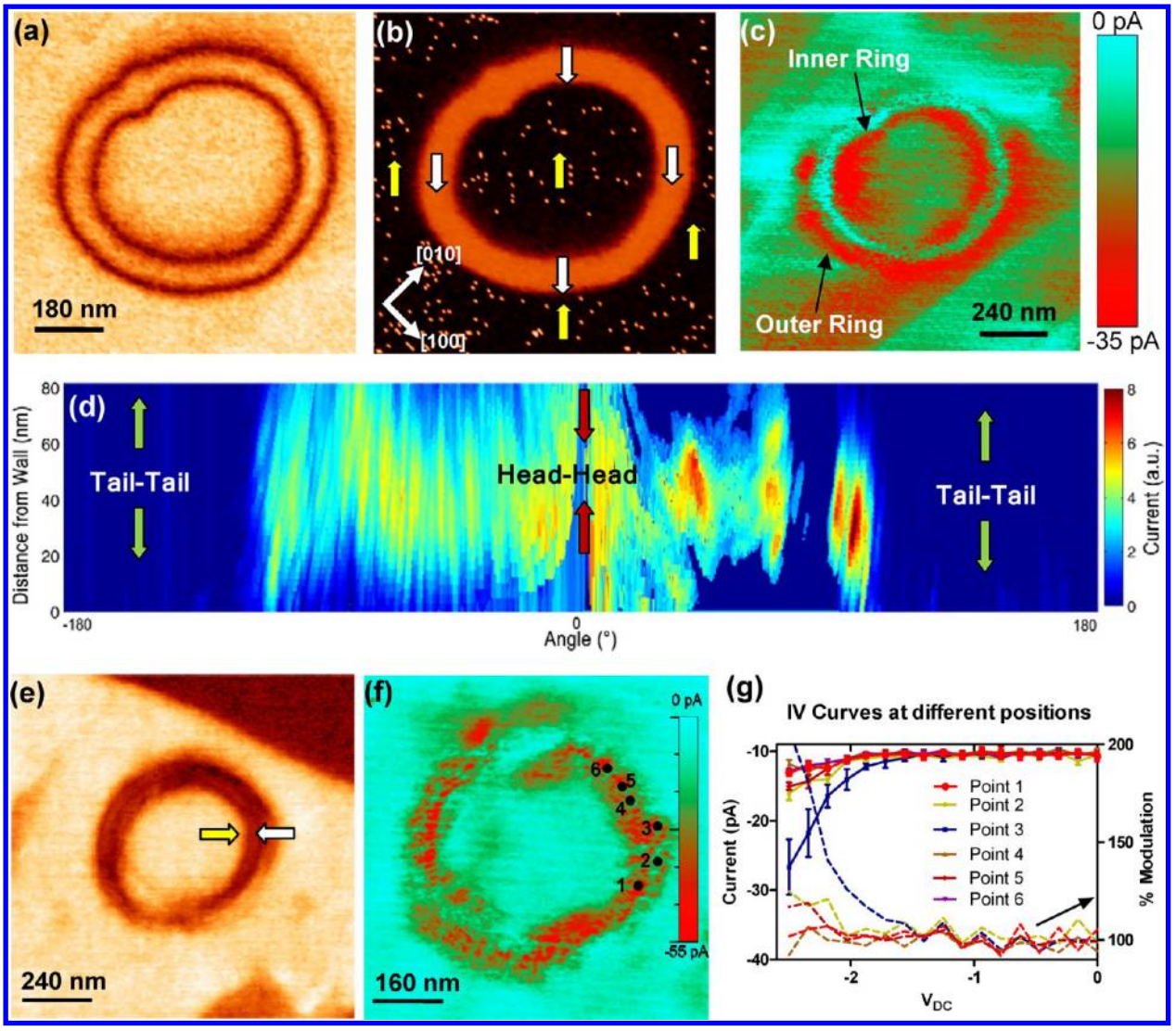

Figure 1. Topological control of conductive states due to tail−tail and head−head charges at the domain wall. (a) Vertical PFM amplitude and (b) phase image of a ring written by +9 V bias within a single lateral domain. The polarization vectors are shown in b. A c-AFM image, taken with V_{tip} = −2.8 V, is shown in c. To better visualize the conduction map, the outer ring in c was flattened to a single 2D map and plotted in d. The experiment was repeated, and I−V curves were captured (e−g). (e) Lateral amplitude PFM and (f) c-AFM image of the same ring, taken with V_{tip} = −2 V. (g) I−V curves taken along different points of the ring, indicated in f.

through control of polarization discontinuities via domain curvature, has remained unexplored.

Here, we explore the tunability of domain wall conductance though orientation control. Domain Walls with varying charge are patterned in a multiferroic $BiFeO_3$ thin-film using a variety of scanning probe microscopy (SPM)-based approaches. I−V measurements show that the conduction through the wall can be modulated at different points along a charged domain wall, depending on the local curvature. In contrast, a straight domain wall shows no variation in conductivity by spatial position. The enhanced conductivity was modeled by analyzing the coupled space charge−polarization dynamics through extended Landau−Ginzburg−Devonshire (LGD) formalism. This analysis suggests that local carrier concentration can be increased by more than an order of magnitude depending on the charge at the wall. Through phase-field modeling, the stability and dynamics of the ring domain structures was explored, which indicates that ring domain structures can possess highly asymmetric potential distributions due to polarization dynamics mediated by elastic effects. These studies provide the first proof of electrical modulation of conduction in the spatial dimension along domain walls in ferroelectric thin-films.

To investigate the dependence of conduction on wall charge, we drew domain patterns in a 200 nm $BiFeO_3$ (BFO) thin film grown on $DyScO_3$ (DSO) with a $SrRuO_3$ (SRO) bottom electrode (thickness 40 nm). The first requirement for the experiment is a large monodomain matrix, in which the curved domain wall can be "written" using a biased SPM tip. Piezoresponse force microscopy (PFM) images reveal that the virgin domain structure of the $BiFeO_3$ film consists of a striped in-plane (IP) domain pattern with mostly 71° walls, with the average stripe width of ∼200 nm and a uniform out-of-plane (OP) polarization vector pointed toward the substrate. To generate larger single domains, we first prepoled squares with the scanning tip held at negative tip bias (V_{tip} = −7 V). This has the effect of effectively doubling the in-plane domain width in the poled area.[27] After selecting a large monodomain region in the poled square, the tip was traced around a circle

dx.doi.org/10.1021/nl302382k | Nano Lett. 2012, 12, 5524−5531

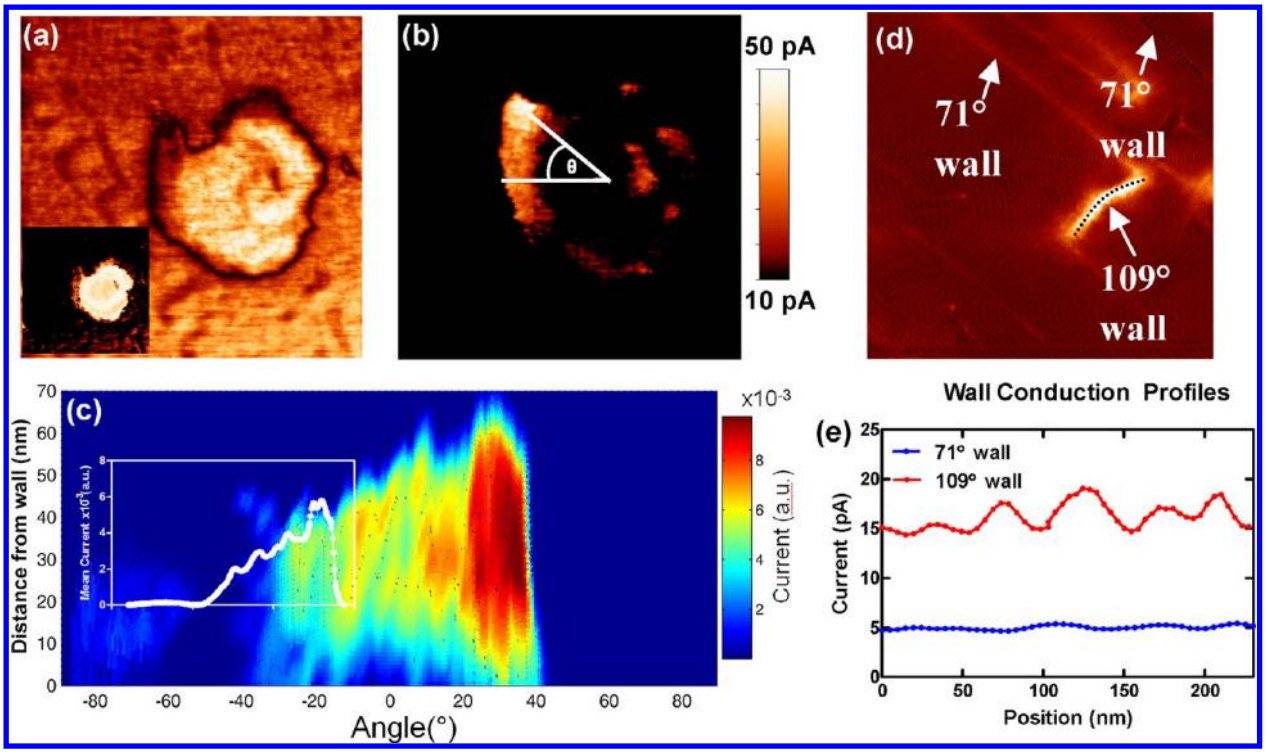

Figure 2. c-AFM of domain structures in vacuum (a) 500 nm × 500 nm vertical PFM amplitude and phase (inset) of a written circular domain pattern. (b) c-AFM of the same region with V_{sample} = +2 V. The conductivity along the outer left edge was smoothed using Gaussian filters and is plotted in c as a function of angle, defined in b, and distance from the domain wall. The mean profile for this plot is shown in the inset. The conductivity of the existing 71° and 109° walls in the film is shown in the 1 μm × 1 μm c-AFM in d, taken with V_{sample} = +1.5 V. Line profiles for the two walls in d are shown in e.

with a bias of +9 V to form the curved walls. The vertical PFM amplitude and phase images as a result of this lithography are shown in Figure 1a and b. Details about the polarization assignment are provided in the Supporting Information, S1; they are marked in Figure 1b. Note that there is a cross talk in the lateral image arising from the collective materials motion across the domain wall.[28−30] The analysis of PFM images indicates that the application of bias forms a 180° wall, in agreement with previous studies.[31]

For the 180° wall, the charge is expected to vary continuously as $2P_s \cos(\theta)$, thus forming head-to-head regions on the bottom side of the ring and tail-to-tail regions on the upper side. The inner wall of the ring is expected to have the opposite charge. The c-AFM scan of this region, with the tip held at V = −2.8 V, is shown in Figure 1c. Notably, the inner and outer walls of the ring structure show different regions of enhanced conductivity. To visualize this behavior more clearly, the conductivity of the outer ring wall was plotted as a function of angle and distance from the domain wall. In forming this plot, we have used a small (∼10 pixel square for a 512 × 512 pixel image) Gaussian filter to smooth the jitter in the conduction map at each pixel. The results, plotted in Figure 1d, show that the conductivity appears to be high at the head-to-head section of the domain wall, while the conductivity drops to zero at the tail−tail section. The inner ring's wall conductivity also appears to follow the same general trend, although the correlation is somewhat less strong.

Having demonstrated that conductivity can be switched simply due to wall charge, we now investigate the degree of variation in the conductance through I−V measurements. I−V curves were captured for a ring written using the same aforementioned approach ,along the head−head region (Supporting Information, S2), shown in Figure 1e−g. The lateral PFM amplitude is shown in Figure 1e, while the c-AFM image of the ring, taken with V_{tip} = −2 V of this ring, is shown in Figure 1f. This displays significant conductivity on the outer parts of the ring on the right-hand side. To determine the I−V characteristics as a function of position, measurements were carried out at six separate points along the ring, marked by black circles in Figure 1f. The measurements were averaged over four separate sweeps and are shown in Figure 1g. As expected, the point of maximum charge (point 3) displays the highest conductivity. The mean percentage modulation of the current was calculated using point 6 as the baseline. The I−V curves show that, with a bias of V = −2.5 V, the current modulation can be significant, depending on position (and correspondingly, charge) along the ring. Importantly, we note here that the origin of the modulation is thermodynamic in nature, with c-AFM maps suggesting the ring is stable for at least several hours.

To minimize the effects of the surface contaminants, similar studies were performed in the ultrahigh vacuum (UHV) environment using an Omicron UHV system equipped with a Nanonis controller. This system is capable of very precise current measurements (down to sub pA range) but does not allow for lateral PFM and offers only limited scan sizes (<5 μm). Due to the lack of lateral PFM, single domains were distinguished by c-AFM. A circular domain structure, written within a single domain, is shown in the vertical amplitude and phase image in Figure 2a. The c-AFM map of this region taken at sample bias of V = +2 V is shown in Figure 2b. Clearly, there appears to be a reduction in current along the domain wall as

dx.doi.org/10.1021/nl302382k | Nano Lett. 2012, 12, 5524−5531

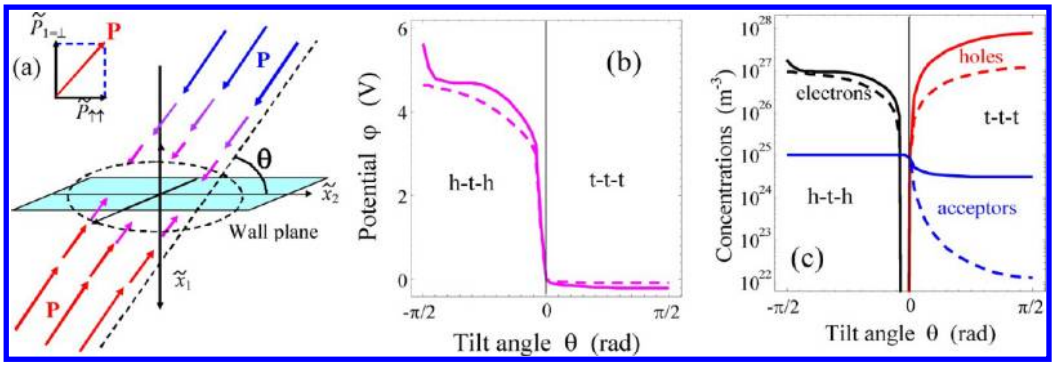

Figure 3. Modeling of a single 180° domain wall in $BiFeO_3$ as a function of tilt angle. (a) One-dimensional distribution of polarization in the vicinity of a single 180° domain wall in $BiFeO_3$. (b) Dependence of potential on the domain wall tilt angle θ. (c) Dependence of electron and hole densities and acceptor concentrations (labels near the curves) on the domain wall tilt angle θ. Solid curves correspond to the maximal values; dashed curves correspond to the values averaged over the wall width (10 nm).

the angle θ (defined in the figure) sweeps through from positive to negative values. To better visualize the conduction map, we plotted the conduction as a function of θ and distance from the domain wall, in Figure 2c, again utilizing a small (~10 pixel square) spatial filter as before. Presuming that the angle is proportional to the charge (as for the ambient experiments), this result proves the ability to modulate conduction through wall charge in ferroelectric thin films. The average current at each value of θ is shown inset. The values show that, in vacuum, it is possible to observe a difference in conduction levels of up to 500% by spatial position alone.

A possibility for the observed anisotropic conductance is the injection of oxygen vacancies by the tip. Yang et al[32] have shown that ionic conductivity from oxygen vacancies in doped BFO films is too low to account for the conduction levels observed here. Additionally, conduction by segregation of tip-injected oxygen vacancies at the domain walls is ruled out by the fact that such a mechanism should be angle independent. Our experiments show that no significant variation in conduction along the straight wall is observed (Fig. 2d,e and Supporting Information, S3), suggesting that even if vacancies are injected inhomogeneously, they likely segregate quickly and cannot account for the anisotropic conduction.

To better understand and explore the thermodynamic origins of the static wall's conductivity, we modeled the space charge accumulation at a prototypical charged 180° ferroelectric domain walls in $BiFeO_3$ using LGD formalism.[23] Since $BiFeO_3$ can be considered a p-type semiconductor,[33] the electrostatic potential φ satisfies the Poisson equation

$$\varepsilon_0\varepsilon_b\Delta\varphi = \mathrm{div}(\mathbf{P}) - e(N_d^+(\varphi) + p(\varphi) - n(\varphi) - N_a^-(\varphi)) \quad (1)$$

Here Δ is the Laplace operator, the charges are in the units of electron charge $e = 1.6 \times 10^{-19}$ C, $\varepsilon_0 = 8.85 \times 10^{-12}$ F/m is the universal dielectric constant, and ε_b is the background dielectric permittivity of the material (unrelated with the soft mode), which is typically much smaller than the ferroelectric permittivity ε_{ij}^f related with the soft mode.

The equilibrium concentrations of ionized donors N_d^+, acceptors N_a^-, free electrons n, and holes p are:

$$N_d^+(\varphi) = N_{d0}(1 - f(E_d - E_F - e\varphi)) = N_{d0}f(-E_d + E_F + e\varphi) \quad (2a)$$

$$N_a^-(\varphi) = N_{a0}f(E_a - E_F - e\varphi) \quad (2b)$$

$$p(\varphi) = \int_0^\infty d\varepsilon \cdot g_p(\varepsilon)f(\varepsilon - E_V + E_F + e\varphi) \quad (2c)$$

$$n(\varphi) = \int_0^\infty d\varepsilon \cdot g_n(\varepsilon)f(\varepsilon + E_C - E_F - e\varphi) \quad (2d)$$

where N_{d0} and N_{a0} are the concentration of donors and acceptors, respectively, $f(x) = \{1 + \exp(x/k_BT)\}^{-1}$ is the Fermi–Dirac distribution function, $k_B = 1.3807 \times 10^{-23}$ J/K, and T is the absolute temperature. E_F is the Fermi level, E_d is the donor level, E_a is the acceptor level, E_C is the bottom of the conductive band, and E_V is the top of the valence band (all energies are defined with respect to the vacuum level). The electron and hole density of states in the effective mass approximation are $g_n(\varepsilon) \approx ((2m_n^3\varepsilon)^{1/2})/(\pi^2\hbar^3)$ and $g_p(\varepsilon) \approx ((2m_p^3\varepsilon)^{1/2})/(\pi^2\hbar^3)$, respectively. Typically the condition $m_n \ll m_p$ is satisfied and $m_p = (5 - 20)m_e$,[32] where m_e is the mass of the free electron. Assuming that a single domain ferroelectric material is electroneutral at zero potential $\varphi = 0$, the condition $N_a^- - N_{d0}^+ = p_0 - n_0$ should be valid. The equilibrium concentrations of donors and acceptors and densities of holes and electrons are defined for the case $\varphi = 0$. Finally, the geometry of the problem and the definition of θ are shown in Figure 3a.

Within LGD formalism (Supporting Information, S4), equations for polarization vector components P_i, elastic strains u_{ij} and stresses σ_{ij} have the form

$$2a_iP_i + 4a_{ijkl}^u P_jP_kP_l - g_{ijkl}\frac{\partial^2 P_k}{\partial x_j\partial x_l} - 2q_{mjki}u_{mj}P_k - f_{mnil}\frac{\partial u_{mn}}{\partial x_l} = -\frac{\partial\phi}{\partial x_l} \quad (3)$$

$$\sigma_{ij} = c_{ijkl}u_{kl} + f_{ijkl}(\partial P_k/\partial x_l) - q_{ijkl}P_kP_l \quad (4)$$

Here a_i and a_{ijkl}^u are LGD free energy expansion coefficients, g_{ijkl} are the gradient energy coefficients, q_{ijkl} is the fourth-rank electrostriction tensor, f_{ijkl} is the fourth-rank tensor of flexoelectric coupling, and c_{ijkl} is the elastic stiffness.

From eqs 1, 3, and 4, it is obvious that electric potential, polarization, and elastic fields are strongly coupled. In particular, the potential will depend strongly on the div(**P**) term, that is, the wall charge. The dependence of the potential on the domain wall tilt angle θ is shown in Figure 3b. It is seen from this figure than the potential barrier and thus carrier accumulation strongly increases with the tilt angle. Tail-to-tail

dx.doi.org/10.1021/nl302382k | Nano Lett. 2012, 12, 5524–5531

(t-t-t) walls are holes accumulating, while head-to-head (h-t-h) walls are electron accumulating as anticipated for a p-type semiconductor-ferroelectric. The asymmetry with respect to $\theta \rightarrow -\theta$ is very strong. Theoretically single crystal BFO should be a p-type semiconductor,[33] which would result in holes being the major carriers and electrons being minor carriers. However, in reality it may be different due to BFO having a complex band structure and especially poorly understood defect chemistry. However, this uncertainty does not affect the model other than on a quantitative level, since the charge of species collecting at the wall is opposite to that of polarization. Also, since the barrier height (for an elementary metal/ferroelectric oxide interface) for holes is much higher than for electrons, the measured currents in these films are predominantly electron currents.[33] If we assume that the conductivity is proportional to the carrier concentration, then from Figure 3c the conductivity should increase by up to 2 orders of magnitude across a fairly narrow range of θ; that is, the onset of conductivity is sudden, reflective of general activated semiconductor transport. Note that the conduction maps in the experiments are taken with sample held at positive voltage with respect to the tip potential, so electrons are the carriers. The relatively narrow range of θ over which local conduction is both detectable and variable may be the reason for the difficulty in observing significant variation in the current along the curved domain wall from c-AFM maps (e.g., Figure 1), particularly in ambient systems.

Profiles of the polarization components normal and parallel to the domain wall, electric potential φ and field E across the domain wall are shown in Figure 4a–d for several tilt angles $\theta = -\pi/2$, $-\pi/4$, 0, $\pi/4$, and $\pi/2$. The potential distribution is symmetric with respect to $\tilde{x}_1 \rightarrow -\tilde{x}_1$ and has a maximum at the wall plane, while the electric field normal component is antisymmetric with respect to $\tilde{x}_1 \rightarrow -\tilde{x}_1$ and also has maxima

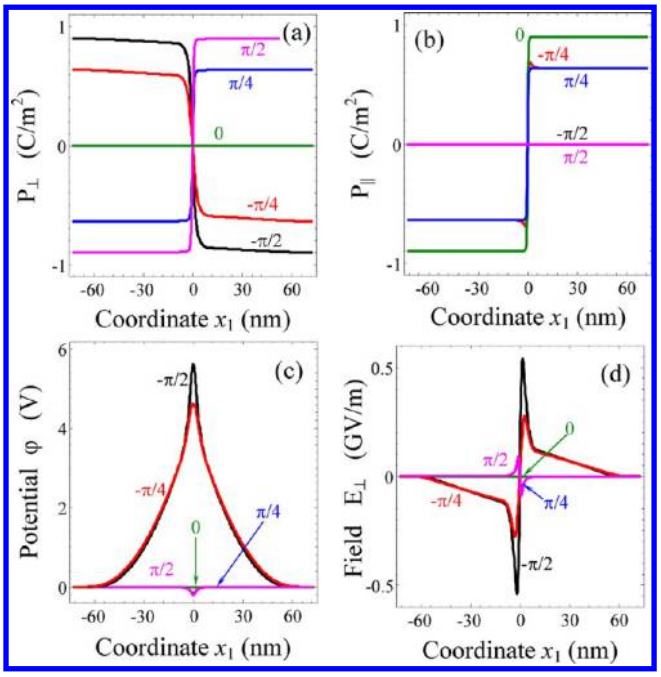

Figure 4. Charge and potential distributions as a function of wall tilt angle. Spatial distribution of the polarization components normal (a) and parallel (b) to the domain wall, electric potential φ (c), and field E (d) across the domain wall calculated for angles $\theta = -\pi/2$, $-\pi/4$, 0, $\pi/4$, and $\pi/2$ (marked near the curves).

near the wall. It is seen from the figure that the potential barrier and electric field amplitude strongly increases with absolute values of θ. Additionally, the asymmetry with respect to $\theta \rightarrow -\theta$ is evident. Finally, Figure 4c shows that significant potential remains at distances ~30 nm on either side of the domain boundary. This fact helps to explain the relatively large width of the conducting regions of domain walls in experiment.

Though the variation in charge around the domain wall can explain the observed conductivity, questions remain as to why such a charged ring structure should form or remain stable. Furthermore, the interplay between the elastic stress redistribution around the ring, and its effect on the polarization over time (especially near the domain wall), cannot be easily explored through SPM, due to inherent resolution limits. Thus, to gain insight into the dynamics of the ring structure and the associated elastic fields and potential distributions, phase-field modeling of the experimental system was undertaken.

The phase-field model[34] (described more completely in Supporting Information, S5) uses the polarization components, P_i, as phase parameters to describe the state of the film. Total system free energy, $F(P_i, P_{i,j})$, expressed as a function of these components and their gradients is minimized by solving the time-dependent Ginzburg–Landau equation for the polarization

$$\frac{\partial P_i}{\partial t} = -L\frac{\delta F(P_j, P_{j,k})}{\delta P_i} \tag{5}$$

In eq 5 L is the kinetic coefficient related to the domain wall mobility. Total system free energy includes contributions from elastic, electric, Landau, and gradient energies, leading to coupled responses, especially between the elastic and electric behavior of the film.[35,36] Equation 5 is solved numerically using the semi-implicit Fourier spectral method.[37]

In this study simulations of both the 180° ring domain structure observed in the film and the nominally uncharged 71° domain wall were conducted to understand the nature of the charge distribution around the ring. Shown in Figure 5a is the initial simulated domain structure for the 180° wall case. Initially, the charge distribution, shown in Figure 5b, was characterized by typical positively charged head-to-head regions (red) and negatively charged tail-to-tail regions (blue). Elastic stresses around the ring were initially constant and due entirely to the coherency strain with the substrate (since the 180° wall is purely ferroelectric, separating two elastically equivalent variants). The domain configuration of the ring domain structure after the ring had been allowed to relax for 500 time steps in the simulation is shown in Figure 5c. In the simulation the polarization evolves to eliminate most bound charges around the ring. Along the [110] direction the ring domain tilted away from the vertical orientation toward the electrically neutral $(11\bar{2})$ plane.[38] Further, several new rhombohedral domains nucleated around the edges of the ring, particularly along the [100] and [010] directions. Together, these changes reduced the overall bound charge in the system. Reduction in electrical energy from relaxation of the ring structure incurred an elastic energy penalty by introducing strains around the ring, resulting in complex interplay between the elastic and electric forces. The inability of the domain walls to relax to completely electrically neutral configuration because of the constraints of the domain shape and coupled response between the introduced elastic stresses and the bound charge accounts for the remaining bound charge around the ring. The

dx.doi.org/10.1021/nl302382k | Nano Lett. 2012, 12, 5524–5531

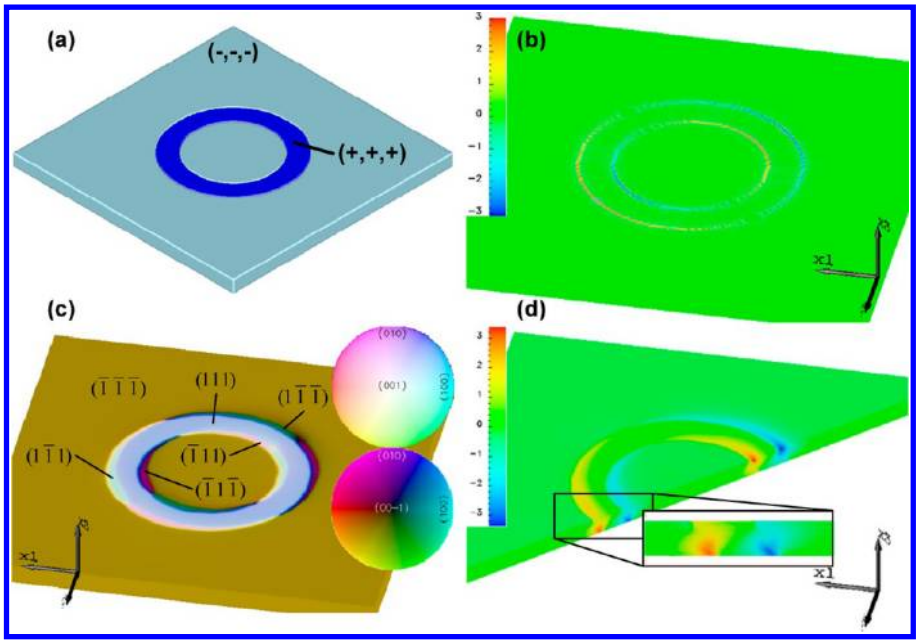

Figure 5. Phase-field simulations of ring domain structure with 180° domain walls. The initial domain configuration assumed to consist of two domains separated by domain walls perpendicular to the substrate is shown in a, and the resulting initial bound charge distribution around the ring is shown in b. After 500 simulation time steps the domain structure has relaxed into a more complex structure with several new domains at the ring edge that compensate part of the bound charge (c). (See Supporting Information S6 for a cross section of the polarization through the film). The potential around the ring after 500 time steps is shown in d with a cut along the $(1\bar{1}0)$ plane to show the potential profile through the thickness of the film. The callout shows an enlarged view of the potential distribution around the domain walls.

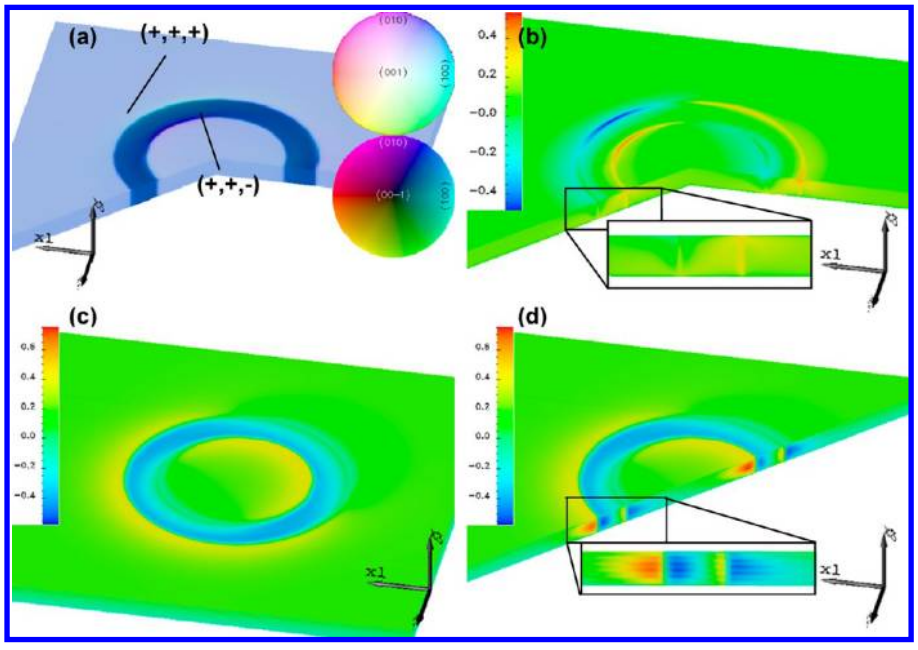

Figure 6. Phase-field simulations of ring domain structure with 71° domain walls. The domain structure of the ring structure after 500 simulation time steps is shown in a with a wedge bounded by the $(1\bar{1}0)$ and (010) planes removed to show the structure through the thickness of the film. The coupling of the elastic stress to change the polarization along the x_1 axis, defined as $\partial f_{elastic}/\partial P_1$, around the ring is shown in b with a wedge bounded by the $(1\bar{1}0)$ and (010) planes removed to show the distribution through the thickness of the film. Callout shows an enlarged view of the distribution around the domain wall. After 500 time steps, elastic stresses cause changes in the magnitude of the polarization at the domain walls, leading to a potential distribution around the ring as shown in c. A cut-away along the $(1\bar{1}0)$ plane shows the potential distribution at the center of the film in d. The callout shows an enlarged view of the potential around the domain wall.

bound charge, elastic stress, and polarization around the ring are discussed in more depth in the Supporting Information, S6.

The potential resulting from the remaining bound charge around the ring at the 500th time step is shown is shown in Figure 5d; areas of low and high potential determine the domain wall's static conductivity by the mechanisms described previously. The potential around the ring appears to agree with the c-AFM images in Figure 1. Additionally, the phase-field simulations allow us to investigate the relative variability of conduction in the *c*-axis of the film by considering the potential

dx.doi.org/10.1021/nl302382k | *Nano Lett.* 2012, 12, 5524−5531

distribution through the thickness of the film, which cannot be probed using SPM. Figure 5d shows the potential distribution on the film on a cut-away through the film along the $(1\bar{1}0)$ plane, revealing that the potential magnitude is largest at the film/electrode interface and near the film surface, decreasing toward the far edge of the film.

Finally, since charged domain walls are associated with a large electrical energy penalty of formation, the possibility of anisotropic conduction at initially *uncharged* domain walls was explored by simulating a similar ring structure with 71° walls. After allowing the system to relax for 500 time steps, the domain walls remained perpendicular to the substrate and therefore nominally uncharged,[38] as shown in Figure 6a. The simulations revealed that, although the initial potential was zero around the ring (as expected), there existed a significant tendency to reduce the elastic energy, $f_{elastic}$, around the ring domain by changing the polarization magnitude, as can be seen in the distribution of $\partial f_{elastic}/\partial P_1$ in Figure 6b (see the Supporting Information S5 and S7 for more details). Elastic energy was reduced in the system by perturbing the polarization locally near the domain walls, creating bound charges on domain walls and associated potentials, as shown on the surface of the film by the potential plot in Figure 6c and in cross section through the film in Figure 6d. Thus, in the case of the 71° ring, the potential build up around the ring is due to a ferroelastic effect where the polarization near the domain wall is disturbed to reduce the high elastic energy at the interface, thus creating bound charges. These studies are pertinent because, though lateral PFM data is absent for the ring structure imaged in Figure 2, the phase-field model predicts that, even without initially charged domain walls, anisotropic potential can develop in these ring geometries, thus leading to spatially modulated conduction.

It is important to note anisotropic conductivity of nominally uncharged ring-shaped walls in thermal equilibrium may also arise from flexoelectric coupling and anisotropic electrostriction, which in turn induces a polarization component perpendicular to the wall plane and thus weakly charges the wall. Other purely strain-related mechanisms such as deformation potential coupled with inhomogeneous strain may also help to explain domain wall conductivity.[39] However, these mechanisms become secondary in magnitude in comparison with the bound charge that develops around the ring, and are therefore not considered in this paper.

The theoretical and experimental results confirm that there exists a significant correlation between wall charge and conductivity, likely due to carriers or vacancies migrating to neutralize the charge at the domain walls and hence locally inducing a transition to a conductive state. Initially it was believed that only 109° and 180° walls were conductive in $BiFeO_3$.[2] However, later experiments have shown that even nominally uncharged 71° walls show some level of conductivity.[15] In experiments carried out in UHV (Figure 2d,e), we have found that, while these walls do indeed conduct, they do so with an order of magnitude less conductivity than the 109° walls. In light of our phase-field simulations, the observation of conduction at the 71° domain walls may be attributed in part to substrate-induced strain and elastic interactions,[40] which cause the domain wall evolution leading to slight bound charge at the domain wall, and thus conductivity as per the thermodynamic mechanisms indicated above. In this sense, the conductivity of the initially uncharged domain wall arises from secondary ferroelastic effects.

Recently, the conductivity within curved, charged walls in the improper ferroelectrics $HoMnO_3$[41] and then $ErMnO_3$[18] has been shown to vary by up to 3 orders of magnitude. To date, controlling the conduction through topological defects in ferroelectrics has been achieved through the field-driven hysteresis arising from dynamic conductivity of the charged interface[17] or 1D channel at fabricated vortex cores.[24] This study shows that the variation in charge at a domain wall as a result of polarization discontinuities, whether they arise through writing of charged structures or through domain wall evolution from an initially uncharged state as a result of secondary ferroelastic effects, presents another option to control the conductivity in the spatial dimension in addition to voltage space in ferroelectrics.

In summary, we have engineered the local conductivity of domain wall as a function of its curvature (and thus charge) using an SPM tip, modeled the phenomenon through Landau−Ginzburg−Devonshire formalism, and studied the polarization dynamics through phase-field simulations. Modulation of current, greater than 200% was achieved through I−V measurements along a charged, curved domain wall, while variation of 500% was observed in c-AFM measurements in UHV conditions. The control of conduction through channels as a function of spatial position presents a new pathway to realizing modulated conduction through insulating ferroelectric materials. Additionally, these studies highlight the promise of controlling the unique functional properties of domain walls along individual isolated walls, thereby greatly expanding the suite of potential applications utilizing domain wall nanoelectronics.

■ ASSOCIATED CONTENT

Supporting Information

Polarization direction assignment (S1), polarization assignment for the second ring (S2), conductivity of a straight domain wall (S3), conductivity of 180° domain walls (S4), phase field modeling (S5), and modeling of the 180° wall (S6) and 71° wall (S7). This material is available free of charge via the Internet at http://pubs.acs.org.

■ AUTHOR INFORMATION

Corresponding Author

*E-mail: nagarajan@unsw.edu.au; sergei2@ornl.gov.

Notes

The authors declare no competing financial interest.

■ ACKNOWLEDGMENTS

R.K.V. and V.N. acknowledge support from the ARC Discovery Project scheme and an Overseas Travel Fellowship by the Australian Nanotechnology Network. E.A.E. and A.N.M. are thankful to NAS Ukraine for support. The research at ORNL (P.M., S.V.K.) was conducted at the Center for Nanophase Materials Sciences, which is sponsored at Oak Ridge National Laboratory by the Division of Scientific User Facilities, U.S. Department of Energy. Computational support for this research for phase field simulations was provided by the Research Computing and Cyberinfrastructure (RCC) group, a unit of ITS at Penn State. J.B. and L.-Q.C. acknowledge funding provided by the Department of Energy Basic Sciences under Grant No. DOE DE-FG02-07ER46417. The work at National Chiao Tung University is supported by the National Science Council, R.O.C (No. NSC-101−2119-M-009−003-MY2),

Ministry of Education (MOE-ATU 101W961), and Center for interdisciplinary science of National Chiao Tung University.

REFERENCES

(1) Parkin, S. S. P.; Hayashi, M.; Thomas, L. *Science* **2008**, *320* (5873), 190−194.
(2) Seidel, J.; Martin, L. W.; He, Q.; Zhan, Q.; Chu, Y. H.; Rother, A.; Hawkridge, M. E.; Maksymovych, P.; Yu, P.; Gajek, M.; Balke, N.; Kalinin, S. V.; Gemming, S.; Wang, F.; Catalan, G.; Scott, J. F.; Spaldin, N. A.; Orenstein, J.; Ramesh, R. *Nat. Mater.* **2009**, *8* (3), 229−234.
(3) Aird, A.; Salje, E. K. H. *Eur. Phys. J. B* **2000**, *15* (2), 205−210.
(4) Salje, E. K. H. *ChemPhysChem* **2010**, *11* (5), 940−950.
(5) Catalan, G.; Seidel, J.; Ramesh, R.; Scott, J. F. *Rev. Mod. Phys.* **2012**, *84* (1), 119−156.
(6) Jiang, W.; Noman, M.; Lu, Y. M.; Bain, J. A.; Salvador, P. A.; Skowronski, M. *J. Appl. Phys.* **2011**, *110*, 034509.
(7) Tselev, A.; Meunier, V.; Strelcov, E.; Shelton, W. A.; Luk'yanchuk, I. A.; Jones, K.; Proksch, R.; Kolmakov, A.; Kalinin, S. V. *ACS Nano* **2010**, *4* (8), 4412−4419.
(8) Lubk, A.; Gemming, S.; Spaldin, N. A. *Phys. Rev. B* **2009**, *80*, 104110.
(9) Goncalves-Ferreira, L.; Redfern, S. A. T.; Artacho, E.; Salje, E.; Lee, W. T. *Phys. Rev. B* **2010**, *81* (2), 024109.
(10) Calleja, M.; Dove, M. T.; Salje, E. K. H. *J. Phys.: Condens. Matter* **2003**, *15* (14), 2301−2307.
(11) Tagantsev, A. K.; Courtens, E.; Arzel, L. *Phys. Rev. B* **2001**, *64*, 224107.
(12) Daraktchiev, M.; Catalan, G.; Scott, J. F. *Phys. Rev. B* **2010**, *81*, 224118.
(13) Lee, D.; Behera, R. K.; Wu, P. P.; Xu, H. X.; Sinnott, S. B.; Phillpot, S. R.; Chen, L. Q.; Gopalan, V. *Phys. Rev. B* **2009**, *80*, 060102.
(14) Marton, P.; Rychetsky, I.; Hlinka, J. *Phys. Rev. B* **2010**, *81*, 144125.
(15) Farokhipoor, S.; Noheda, B. *Phys. Rev. Lett.* **2011**, *107*, 127601.
(16) Maksymovych, P.; Morozovska, A. N.; Yu, P.; Eliseev, E. A.; Chu, Y.-H.; Ramesh, R.; Baddorf, A. P.; Kalinin, S. V. *Nano Lett.* **2011**, *12* (1), 209−213.
(17) Maksymovych, P.; Seidel, J.; Chu, Y. H.; Wu, P.; Baddorf, A. P.; Chen, L.-Q.; Kalinin, S. V.; Ramesh, R. *Nano Lett.* **2011**, *11* (5), 1906−1912.
(18) Meier, D.; Seidel, J.; Cano, A.; Delaney, K.; Kumagai, Y.; Mostovoy, M.; Spaldin, N. A.; Ramesh, R.; Fiebig, M. *Nat. Mater.* **2012**, *11* (4), 284−288.
(19) Guyonnet, J.; Gaponenko, I.; Gariglio, S.; Paruch, P. *Adv. Mater.* **2011**, *23* (45), 5377−5382.
(20) Vul, B. M.; Guro, G. M.; Ivanchik, I. *Ferroelectrics* **1973**, *6* (1−2), 29−31.
(21) Gureev, M. Y.; Tagantsev, A. K.; Setter, N. *Phys. Rev. B* **2011**, *83*, 18.
(22) Eliseev, E. A.; Morozovska, A. N.; Svechnikov, G. S.; Gopalan, V.; Shur, V. Y. *Phys. Rev. B* **2011**, *83* (23), 235313.
(23) Eliseev, E. A.; Morozovska, A. N.; Svechnikov, G. S.; Maksymovych, P.; Kalinin, S. V. *Phys. Rev. B* **2012**, *85* (4), 045312.
(24) Balke, N.; Winchester, B.; Ren, W.; Chu, Y. H.; Morozovska, A. N.; Eliseev, E. A.; Huijben, M.; Vasudevan, R. K.; Maksymovych, P.; Britson, J.; Jesse, S.; Kornev, I.; Ramesh, R.; Bellaiche, L.; Chen, L. Q.; Kalinin, S. V. *Nat. Phys.* **2012**, *8* (1), 81−88.
(25) Balke, N.; Choudhury, S.; Jesse, S.; Huijben, M.; Chu, Y. H.; Baddorf, A. P.; Chen, L. Q.; Ramesh, R.; Kalinin, S. V. *Nat. Nanotechnol.* **2009**, *4* (12), 868−875.
(26) Yi, H. T.; Choi, T.; Choi, S. G.; Oh, Y. S.; Cheong, S. W. *Adv. Mater.* **2011**, *23* (30), 3403.
(27) Chu, Y.-H.; Zhan, Q.; Martin, L. W.; Cruz, M. P.; Yang, P.-L.; Pabst, G. W.; Zavaliche, F.; Yang, S.-Y.; Zhang, J.-X.; Chen, L.-Q.; Schlom, D. G.; Lin, I.-N.; Wu, T.-B.; Ramesh, R. *Adv. Mater.* **2006**, *18*, 2307−2311.
(28) Morozovska, A. N.; Eliseev, E. A.; Bravina, S. L.; Kalinin, S. V. *Phys. Rev. B* **2007**, *75* (17), 174109.
(29) Guyonnet, J.; Bea, H.; Paruch, P. *J. Appl. Phys.* **2010**, *108* (4), 042002.
(30) Guyonnet, J.; Bea, H.; Guy, F.; Gariglio, S.; Fusil, S.; Bouzehouane, K.; Triscone, J. M.; Paruch, P. *Appl. Phys. Lett.* **2009**, *95* (13), 132902.
(31) Zavaliche, F.; Yang, S. Y.; Zhao, T.; Chu, Y. H.; Cruz, M. P.; Eom, C. B.; Ramesh, R. *Phase Trans.* **2006**, *79* (12), 991−1017.
(32) Yang, C. H.; Seidel, J.; Kim, S. Y.; Rossen, P. B.; Yu, P.; Gajek, M.; Chu, Y. H.; Martin, L. W.; Holcomb, M. B.; He, Q.; Maksymovych, P.; Balke, N.; Kalinin, S. V.; Baddorf, A. P.; Basu, S. R.; Scullin, M. L.; Ramesh, R. *Nat. Mater.* **2009**, *8* (6), 485−493.
(33) Dawber, M.; Rabe, K. M.; Scott, J. F. *Rev. Mod. Phys.* **2005**, *77* (4), 1083−1130.
(34) Chen, L.-Q. *J. Am. Ceram. Soc.* **2008**, *91* (6), 1835−1844.
(35) Li, Y. L.; Hu, S. Y.; Liu, Z. K.; Chen, L. Q. *Appl. Phys. Lett.* **2001**, *78* (24), 3878−3880.
(36) Li, Y. L.; Hu, S. Y.; Liu, Z. K.; Chen, L. Q. *Appl. Phys. Lett.* **2002**, *81* (3), 427−429.
(37) Chen, L. Q.; Shen, J. *Comput. Phys. Commun.* **1998**, *108* (2−3), 147−158.
(38) Streiffer, S. K.; Parker, C. B.; Romanov, A. E.; Lefevre, M. J.; Zhao, L.; Speck, J. S.; Pompe, W.; Foster, C. M.; Bai, G. R. *J. Appl. Phys.* **1998**, *83* (5), 2742−2753.
(39) Morozovska, A. N.; Vasudevan, R. K.; Maksymovych, P.; Kalinin, S. V.; Eliseev, E. A. *Phys. Rev. B* **2012**, *86* (8), 085315.
(40) Catalan, G.; Lubk, A.; Vlooswijk, A. H. G.; Snoeck, E.; Magen, C.; Janssens, A.; Rispens, G.; Rijnders, G.; Blank, D. H. A.; Noheda, B. *Nat. Mater.* **2011**, *10* (12), 963−967.
(41) Wu, W.; Horibe, Y.; Lee, N.; Cheong, S. W.; Guest, J. R. *Phys. Rev. Lett.* **2012**, *108* (7), 077203.